AAS 19-280

TRANSIT AND CAPTURE IN THE PLANAR THREE-BODY PROBLEM LEVERAGING LOW-THRUST DYNAMICAL STRUCTURES

Andrew D. Cox*, Kathleen C. Howell† and David C. Folta‡

Path planning in the circular restricted 3-body problem (CR3BP) is frequently guided by the forbidden regions and manifold arcs. However, when low-thrust is employed to modify the spacecraft trajectory, these dynamical structures pulsate with the varying Hamiltonian value. In a combined CR3BP, low-thrust (CR3BP-LT) model, an additional low-thrust Hamiltonian is available that remains constant along low-thrust arcs. Accordingly, the analogous low-thrust forbidden regions and manifolds are static and are useful guides for low-thrust trajectory design. Strategies leveraging these structures and other insights from the CR3BP-LT are explored to construct transit and capture itineraries.

INTRODUCTION

A variety of upcoming missions plan to leverage low-thrust propulsion capabilities to enable transfers between Earth and the Moon. For example, current designs for the Deep Space Gateway rely on low-thrust propulsion to deliver supplies from the Earth to an outpost located in a near rectilinear halo orbit near the Moon.[?] Another example is the Lunar IceCube spacecraft, one of several small satellites to be launched as secondary payloads with Exploration Mission 1; Lunar IceCube will employ a low-thrust engine to reach a polar orbit about the Moon.[1] Accordingly, trajectory design strategies that employ low-thrust to transit between the Earth and Moon are the focus of this investigation. More specifically, strategies that leverage dynamical structures from the low-thrust-enabled circular restricted 3-body problem (CR3BP-LT) to accomplish such transfers are examined.

Many authors have investigated similar ballistic transfers in the circular restricted 3-body problem (CR3BP). It is well-established that the invariant manifolds associated with planar periodic orbits located in the forbidden region gateways act as separatrices between transit and non-transit motion at the the gateway.[2] Thus, by selecting trajectory arcs that pass within the manifold boundaries, transfers that navigate through the L_1 or L_2 gateways to reach the secondary body, P_2, (e.g., the Moon in the Earth-Moon CR3BP) are straightforwardly designed.[3,4] Low-thrust has previously been applied to these ballistic transfers to achieve a final state near P_2; optimization methods are also utilized to identify a suitable low-thrust control history.[5,6] However, rather than initialize trajectory designs with dynamical structures from the ballistic CR3BP, structures from the CR3BP-LT are employed in this analysis. This approach offers several advantages over strategies that include only

*Ph.D. Student, School of Aeronautics and Astronautics, Purdue University, West Lafayette, IN 47907; cox50@purdue.edu
†Hsu Lo Distinguished Professor of Aeronautics and Astronautics, School of Aeronautics and Astronautics, Purdue University, West Lafayette, IN 47907; howell@purdue.edu
‡Senior Fellow, NASA Goddard Space Flight Center, Greenbelt, MD, 20771; david.c.folta@nasa.gov

ballistic structures. First, a trajectory leveraging the low-thrust structures provides a more accurate solution; the addition of a low-thrust acceleration to a trajectory following ballistic structures may change the properties along the dynamical path, nullifying the original reason for the inclusion of the ballistic structures in the solution. Second, an initial guess with low-thrust structures includes a control history, thus, the control parameters or costates are available. Finally, while ballistic structures maintain a fixed energy, the low-thrust dynamical structures supply paths through energy space. As a result, the low-thrust arcs may simultaneously adjust the spacecraft position, velocity, and energy, potentially reducing the flight time required to reach a set of geometric and energetic targets.

Rather than focusing on optimality (e.g., minimizing flight time or maximizing fuel mass), this investigation develops strategies that leverage low-thrust dynamical structures to yield initial solutions with fully-defined control histories; such solutions may be employed to initialize optimization methods in later stages of the design process. To support current and future missions, the dynamics of the Earth-Moon CR3BP-LT are explored to design trajectories that link the Earth, the Moon, as well as translunar regions. One useful set of dynamical structures are the low-thrust forbidden regions, similar to the natural CR3BP forbidden regions, that bound the low-thrust motion and supply the minimum energy requirements for transit. Similarly, the manifolds associated with low-thrust planar periodic orbits in the forbidden region gateways act as separatrices between transit and non-transit behavior, supplying additional geometric constraints.[7,8] Thus, low-thrust trajectories that transit one or both of the gateways are constructed by selecting low-thrust arcs that flow through these manifolds. Itineraries that include multiple gateway transits are constructed by applying Poincaré mapping techniques, allowing each segment to be designed independently. Several sample trajectories that capture near the Moon or transit the lunar region are included to illustrate these design strategies.

DYNAMICAL MODELS

The first step in computing and leveraging dynamical structures within the CR3BP-LT is the development of the dynamical model. An energy-based approach is first employed to derive the governing equations in the CR3BP and obtain an expression for the natural Hamiltonian. By augmenting the CR3BP equations of motion (EOMs) with a low-thrust term, the CR3BP-LT is constructed and the associated low-thrust Hamiltonian is defined. Simplifying assumptions applied to the CR3BP-LT yield a conservative, autonomous system with properties that may be leveraged to facilitate low-thrust trajectory designs.

Circular Restricted 3-Body Problem

The CR3BP describes the motion of a relatively small body, such as a spacecraft, in the presence of two larger gravitational point masses (P_1 and P_2) with paths that evolve along circular orbits about their mutual barycenter (B). To simplify the governing equations and enable straightforward visualization of periodic solutions, the motion of the spacecraft is described in a right-handed frame ($\hat{x},\ \hat{y},\ \hat{z}$) that rotates with the two primaries, as seen in Figure 1, where $\hat{x}$, $\hat{y}$, and $\hat{z}$ are vectors of unit length. The system is parameterized by the mass ratio, $\mu = M_2/(M_1+M_2)$, where M_1 and M_2 are the masses of the primaries and $M_1 \geq M_2$. To facilitate numerical integration, the dimensional values are nondimensionalized by characteristic quantities such that the distance between P_1 and P_2 is unity, the mean motion of the two primaries is unity, and the masses of each body range from zero to one.[9] The spacecraft is located relative to the system barycenter in the rotating frame via the

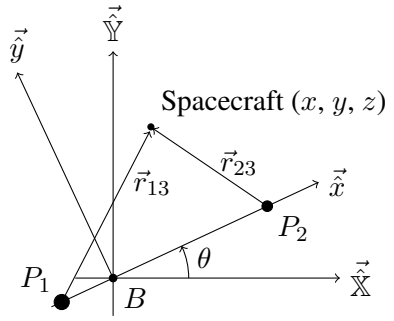

Figure 1. CR3BP system configuration; two point masses, P_1 and P_2, proceed on circular orbits about their mutual barycenter, B. The behavior of a third, relatively massless particle is described within the rotating coordinate frame, ($\hat{x},\ \hat{y},\ \hat{z}$)

vector $\vec{r} = \{x\ \ y\ \ z\}^T$.

The equations of motion governing the CR3BP are derived via a Hamiltonian energy approach. Let the *natural Hamiltonian* be expressed as

$$H_{nat} = \frac{1}{2}v^2 - \frac{1}{2}\left(x^2 + y^2\right) - \frac{1-\mu}{r_{13}} - \frac{\mu}{r_{23}}\,, \tag{1}$$

where r_{13} and r_{23} are the distances between the spacecraft (P_3) and the two primaries,

$$r_{13} = \sqrt{(x+\mu)^2 + y^2 + z^2}\,, \qquad r_{23} = \sqrt{(x-1+\mu)^2 + y^2 + z^2}\,,$$

and v is the magnitude of the rotating velocity vector, $v^2 = \dot{x}^2 + \dot{y}^2 + \dot{z}^2$. By applying Hamilton's canonical equations of motion, a set of differential equations that govern the motion of P_3 emerges,

$$\ddot{x} = 2\dot{y} + \Omega_x, \tag{2}$$

$$\ddot{y} = -2\dot{x} + \Omega_y, \tag{3}$$

$$\ddot{z} = \Omega_z, \tag{4}$$

where Ω is the CR3BP *pseudo-potential* function,

$$\Omega = \frac{1}{2}(x^2 + y^2) + \frac{1-\mu}{r_{13}} + \frac{\mu}{r_{23}}\,, \tag{5}$$

and Ω_x, Ω_y, and Ω_z represent the partial derivative of Ω with respect to the subscripted state variables x, y, and z, respectively. Because the CR3BP is autonomous and conservative, H_{nat} is constant and equivalent to the Jacobi integral, i.e., the *Jacobi constant*. The Jacobi constant, $C = -2H_{nat}$, is commonly leveraged as a measure of the energy associated with arcs in the CR3BP.

CR3BP Incorporating Low-Thrust

To incorporate low-thrust into the CR3BP, the low-thrust acceleration vector is first defined. This vector,

$$\vec{a}_{lt} = a_{lt}\hat{u}\,, \tag{6}$$

is oriented relative to the rotating frame via the unit vector $\hat{u}$ and scaled by the nondimensional acceleration magnitude, $a_{lt} = f/m$. In this expression, f represents the nondimensional thrust

magnitude and m is the nondimensional spacecraft mass, $m = M_3/M_{3,0}$, where M_3 is the instantaneous spacecraft mass and $M_{3,0}$ is the initial (wet) spacecraft mass. To apply an energy-based derivation of the CR3BP-LT EOMs similar to the derivation leveraged for the CR3BP, the CR3BP dynamics are augmented with a low-thrust acceleration term. The resulting *low-thrust Hamiltonian* is

$$H_{lt} = \frac{1}{2}v^2 - \frac{1}{2}\left(x^2 + y^2\right) - \frac{1-\mu}{r_{13}} - \frac{\mu}{r_{23}} - \vec{r}\bullet\,\vec{a}_{lt}\,, \tag{7}$$

which may also be written in terms of the natural Hamiltonian, i.e.,

$$H_{lt} = H_{nat} - \vec{r}\bullet\,\vec{a}_{lt}\,. \tag{8}$$

Due to the time-varying nature of the spacecraft mass, m, the governing equations are not available directly from Hamilton's canonical equations. However, Newton's law may be applied to yield the EOMs,

$$\ddot{x} = 2\dot{y} + \Omega_x + a_{lt}u_x, \tag{9}$$

$$\ddot{y} = -2\dot{x} + \Omega_y + a_{lt}u_y, \tag{10}$$

$$\ddot{z} = \Omega_z + a_{lt}u_z, \tag{11}$$

$$\dot{m} = \frac{-fl_*}{I_{sp}g_0t_*}, \tag{12}$$

where u_x, u_y, and u_z are the individual components of $\hat{u}$ along each of the rotating axes, l_* and t_* are the characteristic length and time quantities that nondimensionalize the CR3BP-LT coordinates, I_{sp} is the specific impulse associated with the propulsion system, and $g_0 = 9.80665\text{e-}3$ km/s^2. These equations are consistent with those that govern the natural CR3BP and are simply augmented with the low-thrust acceleration terms.

CR3BP-LT Simplifications for Global Insight

To facilitate analyses in the CR3BP-LT, simplifications are applied to reduce the number of dimensions. The conservative, natural problem admits an integral of the motion (the Hamiltonian, H_{nat}), reducing the natural problem dimension by one. However, due to the non-autonomous nature of the CR3BP-LT, the low-thrust Hamiltonian is not constant in general and, thus, does not necessarily offer a similar dimension reduction in the low-thrust problem. Nevertheless, an analysis of the time derivative of the low-thrust Hamiltonian supplies useful insights. First, differentiate the first term in Equation (8), i.e., the expression for the natural Hamiltonian,

$$\frac{\partial H_{nat}}{\partial \tau} = \dot{x}\left(\ddot{x} - \Omega_x\right) + \dot{y}\left(\ddot{y} - \Omega_y\right) + \dot{z}\left(\ddot{z} - \Omega_z\right)\,. \tag{13}$$

Substitute the CR3BP-LT equations of motion from Equations (9) – (12) into this derivative expression and simplify:

$$\frac{\partial H_{nat}}{\partial \tau} = \dot{x}\left(2\dot{y} + a_{lt}u_x\right) + \dot{y}\left(-2\dot{x} + a_{lt}u_y\right) + \dot{z}a_{lt}u_z = \vec{v}\bullet\,\vec{a}_{lt}\,, \tag{14}$$

where $\vec{v} = \{\dot{x}\ \ \dot{y}\ \ \dot{z}\}^T$ is the spacecraft velocity vector in the rotating frame. The derivative of the second term in Equation (8) is straightforwardly evaluated,

$$\frac{\partial}{\partial \tau}\left[\vec{r}\bullet\,\vec{a}_{lt}\right] = \vec{v}\bullet\,\vec{a}_{lt} + \vec{r}\bullet\,\dot{\vec{a}}_{lt}\,. \tag{15}$$

Combine Equations (14) and (15) to yield the time derivative of H_{lt},

$$\frac{\partial H_{lt}}{\partial \tau} = -\vec{r} \cdot \dot{\vec{a}}_{lt} \,. \tag{16}$$

If $\vec{a}_{lt}$ is constant, both in magnitude and orientation as viewed in the rotating frame, $\dot{\vec{a}}_{lt} = \vec{0}$ and H_{lt} is constant during low-thrust propagations. That is, if $\vec{a}_{lt}$ is constant, the CR3BP-LT is a conservative system and the low-thrust Hamiltonian may be leveraged as an integral of the motion in the low-thrust problem.

While preserving a fixed orientation, i.e., a fixed $\hat{u}$ vector, is a familiar attitude control strategy, preserving a constant acceleration magnitude, a_{lt}, is less common. Consider the expression, $a_{lt} = f/m$ with a fixed orientation and a fixed thrust magnitude ($\hat{u}$ = constant, f = constant) but with variable mass. Accordingly, the time derivative of $\vec{a}_{lt}$, evaluated as

$$\dot{\vec{a}}_{lt} = \frac{f\dot{m}}{m^2}\hat{u} = -a_{lt}^2 \frac{l_*}{I_{sp} g_0 t_*}\hat{u} \,, \tag{17}$$

is non-zero when $\dot{m} \neq 0$. To determine if the derivative magnitude, $\dot{a}_{lt} = -a_{lt}^2 l_*/(I_{sp} g_0 t_*)$, is sufficiently small to be ignored, compare $\dot{a}_{lt}$ with the energy range across the natural equilibrium solutions, i.e., the H_{nat} values associated with the CR3BP Lagrange points. In the Earth-Moon CR3BP-LT, this energy range, $H_{nat}(L_5) - H_{nat}(L_1)$, where L_5 and L_1 are the natural equilibria with the highest and lowest energies, respectively, is several orders of magnitude larger than $\dot{a}_{lt}$. Subsequently, the variations in H_{lt} due to the time-varying spacecraft mass are very small compared to the $L_5 \rightarrow L_1$ energy range, and H_{lt} is reasonably approximated as a constant for propagations with a maximum mass consumption of 15%, i.e., propagations with $m(\tau) > 0.85$. However, this assumption is not applicable to all three-body systems, particularly those with large l_*/t_* ratios (resulting in a large $\dot{\vec{a}}_{lt}$ magnitude) and those with very small $L_5 \rightarrow L_1$ energy ranges, e.g., the Sun-Earth system. In such systems, the characteristic quantities may be adjusted to produce an l_*/t_* ratio that sufficiently decreases the magnitude of the H_{lt} derivative. As the analyses in this investigation leverage the dynamics of the Earth-Moon system, a_{lt} and H_{lt} are assumed constant without adjustment of the characteristic quantities such that the resulting dynamical properties may be leveraged to inform the low-thrust trajectory design problem. Accordingly, the variable acceleration quantity f/m is replaced by the constant value a_{lt}, removing the need for the mass time-derivative in Equation (12). These simplifications – a constant low-thrust Hamiltonian and a constant acceleration magnitude – effectively reduce the problem dimension by two.

By leveraging the simplifying assumption of a constant low-thrust acceleration vector, additional insights are available to guide low-thrust trajectory design. Although H_{nat} does not represent a dynamically significant quantity in the CR3BP-LT (rather, it is merely a component of the low-thrust Hamiltonian, expressed in Equation (7)), it remains a useful reference to the natural CR3BP. Low-thrust arcs are frequently a means to transition between natural structures with fixed H_{nat} values, thus, the evolution of H_{nat} in the CR3BP-LT is relevant. While H_{nat} is not constant in general when low-thrust is active, H_{nat} evolves independently of the spacecraft path when $\vec{a}_{lt}$ is fixed in the rotating frame. This property is available from the time-derivative of H_{nat}, expressed in Equation (14). As the $\vec{a}_{lt}$ vector is constant, this expression is integrable, yielding the equation

$$H_{nat}(\tau_f) - H_{nat}(\tau_0) = \int_{\tau_0}^{\tau_f} \vec{v} \cdot \vec{a}_{lt} \, \mathrm{d}\tau = (\vec{r}(\tau_f) - \vec{r}(\tau_0)) \cdot \vec{a}_{lt} \,. \tag{18}$$

Accordingly, the natural Hamiltonian value along any low-thrust arc is available given the initial H_{nat} value, the initial and final position, and the fixed low-thrust acceleration vector. This relationship supplies useful insights that link the geometry of low-thrust arcs to the evolution of H_{nat}, facilitating intuitive design strategies.

Finally, to further reduce the system complexity, only planar motion is explored. Thus, $z(\tau) = \dot{z}(\tau) = 0$ for all τ, and the low-thrust pointing vector, $\hat{u}$, is described by the planar vector

$$\hat{u} = \begin{Bmatrix} \cos\alpha & \sin\alpha & 0 \end{Bmatrix}^T . \tag{19}$$

These simplifications facilitate the analysis of dynamical structures in the CR3BP-LT while also supplying insights that are useful for spatial (3D) path planning.

LOW-THRUST DYNAMICAL STRUCTURES

The autonomous, Hamiltonian CR3BP-LT (with a constant low-thrust acceleration vector, $\vec{a}_{lt}$) admits a variety of dynamical structures that prove useful for low-thrust trajectory design applications. The equilibrium solutions supply an initial characterization of the local and global dynamics. Low-thrust forbidden regions, similar to the CR3BP forbidden regions, bound low-thrust flow at a specific H_{lt} value and possess gateways at the equilibrium points. A variety of periodic orbits exist near the equilibria; the manifolds associated with these periodic solutions act as separatrices, bounding low-thrust arcs that pass through the gateways that emerge near the equilibrium points as the boundaries of the forbidden regions recede. Accordingly, these structures guide transit and capture motion. A brief exploration of each of these structures is included.

Equilibrium Points and the Forbidden Regions

The equilibrium solutions in the CR3BP-LT supply an initial characterization of the local and global dynamics near the low-thrust forbidden region gateways (hereafter shortened to low-thrust gateways). In the ballistic CR3BP, five equilibrium solutions exist: the L_1, L_2, and L_3 points located on the rotating $\hat{x}$-axis, and the L_4 and L_5 points off-axis in the xy-plane.[9] When a low-thrust force is included in the model, the equilibrium solutions are perturbed from the ballistic solutions, as depicted in Figure 2 for the planar Earth-Moon CR3BP-LT. In this example, the low-thrust acceleration magnitude is $a_{lt} = 7\text{e-}2$ nondimensional units, or approximately 0.19 mm/s^2. The low-thrust planar equilibria move throughout the xy-plane as α varies; this variation is visually represented by the color of the points. Three distinct contours of equilibria are depicted and labeled $\mathbb{E}_1$, $\mathbb{E}_2$ and $\mathbb{E}_3$. Each of these contours represents a set of locations where the net acceleration acting on the spacecraft sums to zero; accordingly, each curve is termed a *zero acceleration contour*.[8,10]

As the focus of this current work is the motion near P_2, the $\mathbb{E}_1$ and $\mathbb{E}_2$ equilibrium point sets are of particular interest. While the locations of the low-thrust equilibria on $\mathbb{E}_3$ vary significantly from the ballistic L_3, L_4, and L_5 locations with α, the $\mathbb{E}_1$ and $\mathbb{E}_2$ equilibria remain nearby the original L_1 and L_2 across the full range of α values, as depicted in Figure 2(b). Furthermore, the linear stability properties of these low-thrust equilibria are qualitatively identical to the L_1 and L_2 linear stability properties; the planar dynamics near the points are consistently characterized by a two-dimensional center mode and a two-dimensional saddle mode. Recall that the center mode associated with the L_1 and L_2 solutions offers an initial approximation for the well-known Lyapunov orbits in the natural CR3BP.[9] Similarly, periodic solutions in the CR3BP-LT are predicted by the existence of the center mode associated with the $\mathbb{E}_1$ and $\mathbb{E}_2$ equilibria.[7,10] The saddle mode approximates unstable and

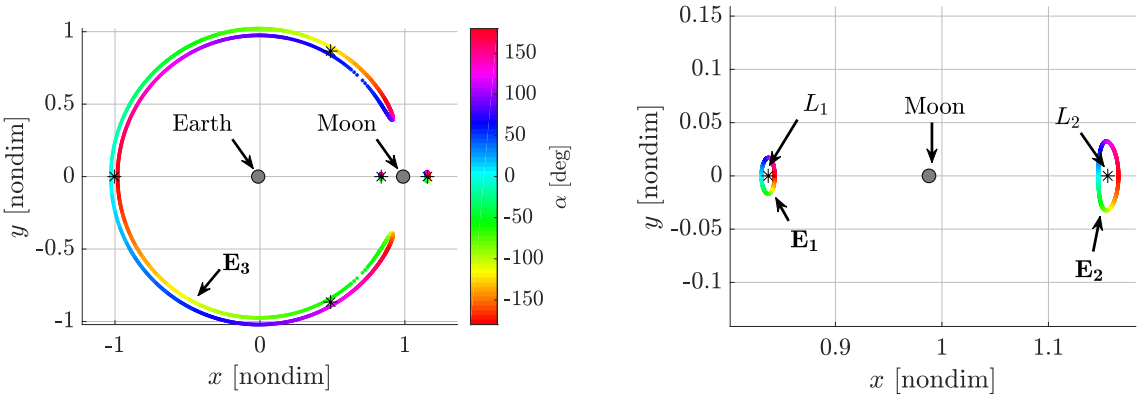

(a) Low-thrust equilibria throughout the system

(b) A close-up view of the $\mathbb{E}_1$ and $\mathbb{E}_2$ low-thrust equilibria (colored) near the natural L_1 and L_2 points

Figure 2. Low-thrust equilibrium solutions (colored by α) in the Earth-Moon CR3BP-LT for $a_{lt} = 7$e-2 and $\alpha \in [-\pi, \pi]$; the natural equilibrium solutions are included as black asterisks.

stable manifolds that asymptotically approach the equilibrium point in forward and reverse time, respectively. By incorporating these manifolds into a trajectory design, the spacecraft is guided to and from the equilibria, i.e., to and from the low-thrust gateways.[11,12] Thus, an understanding of the dynamics near the equilibria is an important step in understanding the dynamical structures available in the CR3BP-LT.

A brief exploration of the Hamiltonian values associated with the equilibria is an important step in facilitating transit near P_2. One useful visualization is a plot of the low-thrust Hamiltonian values of the zero acceleration contours (ZACs) as a function of the thrust angle, α, as appears in Figure 3. A vertical line at a particular α value identifies the H_{lt} values associated with the equilibrium points, i.e., each intersection between this line and the ZACs identifies a distinct equilibrium point. As in the ballistic case, the forbidden regions in the low-thrust model possess gateways at the equilibria and each gateway opens or closes at the H_{lt} value associated with the equilibrium point. For example, at $\alpha = 0$ and $H_{lt} < -1.7$, all of the low-thrust gateways are closed. As H_{lt} increases, the $E_2(\alpha = 0)$ gateway opens at $H_{lt} = -1.67$, followed by the $E_1(0)$ gateway at $H_{lt} = -1.653$. Note that these low-thrust gateways open in the opposite order as the natural gateways; in the ballistic CR3BP, the L_1 gateway opens before the L_2 gateway. Thus, the gateway energy order is a function of the low-thrust parameters.

The energy curve representation of the equilibrium points supplies bounds on the low-thrust parameters that govern transit and capture motion. A spacecraft can only pass through both gateways when the H_{lt} value on the trajectory is sufficiently high, i.e., when the H_{lt} and α quantities locate a point above the $\mathbb{E}_1$ and $\mathbb{E}_2$ energy curves. Similarly, a low-thrust arc that transits one gateway but not the other may be identified by selecting a low-thrust Hamiltonian value and an α angle that locate a point between the $\mathbb{E}_1$ and $\mathbb{E}_2$ energy curves.[8] Thus, this analysis of the CR3BP-LT equilibria and their associated H_{lt} values provides insights to guide low-thrust transit and capture designs. However, while these energy boundaries are sufficient to prohibit transit when a gateway is closed, a higher H_{lt} value does not guarantee transport through a gateway; additional geometric factors must be considered.

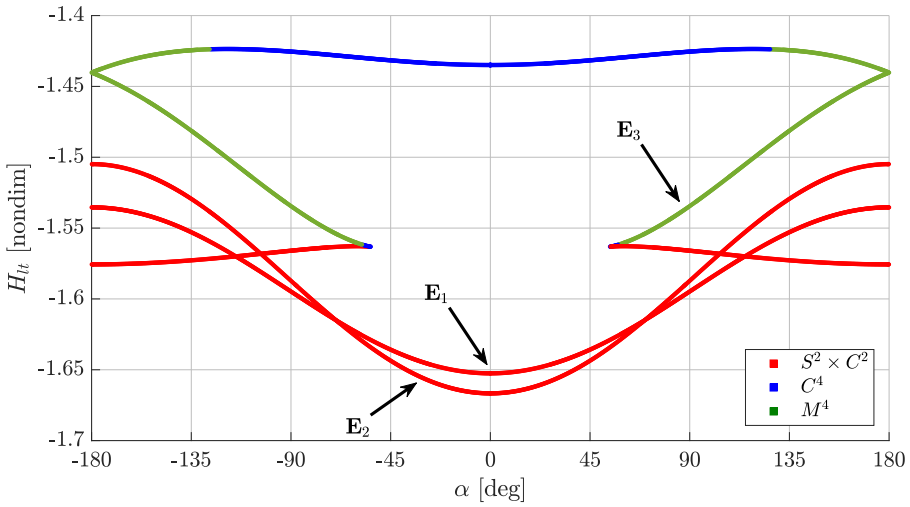

Figure 3. The low-thrust Hamiltonian values associated with the three ZACs; points are colored by the planar stability properties of the linear modes: S^2 indicates a 2D saddle mode, C^4 indicates a 4D center mode, and M^4 indicates a 4D "mixed" mode, i.e., a mode with both oscillatory and asymptotic trends.

Periodic Orbits and Their Manifolds

A variety of low-thrust periodic orbits exist in the vicinity of the low-thrust equilibrium points. Recall that the dynamics in the simplified CR3BP-LT employed in this investigation are autonomous and conservative. As a result, many of the dynamical systems tools commonly employed in the natural CR3BP may be applied to the CR3BP-LT, including techniques to initialize and continue families of periodic orbits. Let a low-thrust periodic orbit (LTPO) be represented by $\Gamma(\tau)$, where $\tau \in [0, T)$ represents the time along the orbit and T is the period of the orbit. To construct a single periodic orbit near an equilibrium point, an initial approximation is leveraged from the linear dynamics and corrected for periodicity via a differential corrections process. The solution is parameterized by the a_{lt} magnitude, the α angle, and the H_{lt} value on the orbit, all of which remain constant over τ. Thus, $\Gamma = \Gamma(\tau; a_{lt}, \alpha, H_{lt})$. In this investigation, a_{lt} is consistently defined as $a_{lt} = 7\text{e-}2$ (approximately 0.19 mm/s^2), thus, a_{lt} is omitted from the parameter list. The τ parameter is also excluded for brevity, yielding $\Gamma = \Gamma(\alpha, H_{lt})$.

Similar to the equilibrium solutions, which are fixed points in the rotating frame, Γ may be represented as a fixed points on a stroboscopic map. A linearization of the dynamics on this map about the periodic orbit fixed point, i.e., the *monodromy matrix*, $\mathbf{\Phi}(\tau + T, \tau)$ supplies insights about flow near Γ.[13] More specifically, the eigenvalues of $\mathbf{\Phi}$ provide stability information and the eigenvectors of $\mathbf{\Phi}$ span the subspaces associated with the various stability modes. Because the CR3BP-LT employed in this investigation is autonomous and Hamiltonian, $\mathbf{\Phi}$ possesses two unit eigenvalues.[9] The remaining four eigenvalues represent either saddle or center modes and the associated eigenvectors span the saddle and center subspaces. The saddle subspace is commonly represented by the stable and unstable manifolds, W^S and W^U, that asymptotically approach the originating periodic orbit in forward and reverse time, respectively. In the ballistic, planar CR3BP, these manifolds act as four-dimensional separatrices: Trajectories cannot pierce either manifold, and the manifolds cannot self intersect. These manifolds associated with periodic orbits located in the gateways also span the four-dimensional forbidden region boundaries, thus, all transit motion must pass through the

manifolds.[2] The manifolds associated with the planar LTPOs appear to possess similar separatrix properties as the natural periodic orbit manifolds.[8] Therefore, trajectories that transit the low-thrust forbidden region gateways pass through the LTPO manifolds.

As LTPOs exist for a range of α and H_{lt} values, a first step in identifying transit options is an exploration of the stability properties of the LTPOs. Additionally, since the focus of this work is transit through the P_2 region, only LTPOs within the center subspace of the $\mathbb{E}_1$ and $\mathbb{E}_2$ equilibrium points are considered. These orbits, plotted in "energy space" in Figure 4, are bounded by the ZAC energy curves, plotted in gray. Such a representation is intuitive since an equilibrium point energy

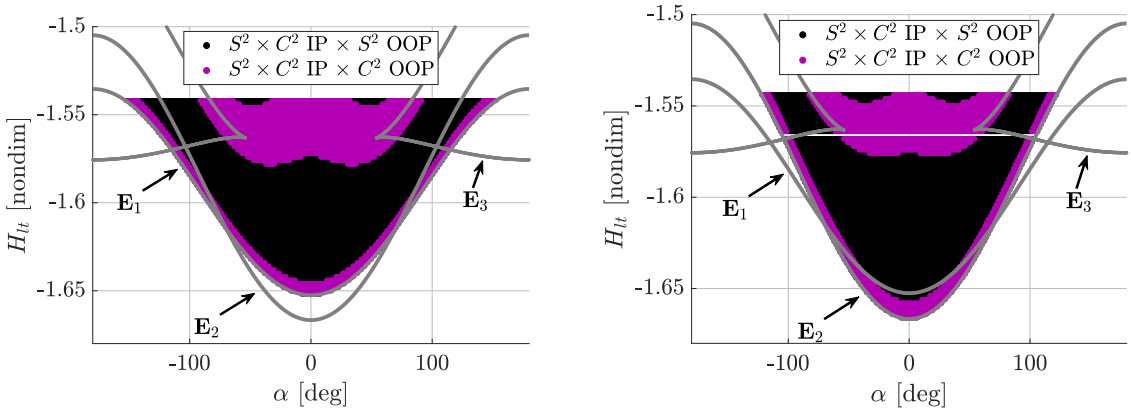

(a) $\mathbb{E}_1$ LTPOs

(b) $\mathbb{E}_2$ LTPOs

Figure 4. Families of low-thrust periodic orbits (LTPOs) centered on the $\mathbb{E}_1$ and $\mathbb{E}_2$ equilibria in the Earth-Moon CR3BP-LT with a_{lt} = 7e-2 for a variety of α and H_{lt} values. Each orbit is colored by its in-plane (IP) and out-of-plane (OOP) stability properties.

curve identifies the H_{lt} value at which the gateway closes for each α angle; at lower H_{lt} values, the gateway is closed and motion is forbidden at or nearby the equilibrium point. Thus, the E_1 and E_2 orbits exist only above the $\mathbb{E}_1$ and $\mathbb{E}_2$ energy curves. The color of each orbit in Figure 4 denotes the linear stability properties. Similar to the $\mathbb{E}_1$ and $\mathbb{E}_2$ energy curves, the in-plane stability properties (abbreviated as "IP" in the figure legends) of each LTPO are described by the superposition of a 2D saddle subspace (S^2) and a 2D center subspace (C^2). This C^2 subspace describes the LTPO and the LTPO family, while the S^2 subspace contains the planar stable and unstable manifolds. Because this S^2 subspace is common to all of the LTPOs, manifolds to guide flow through the $E_1(\alpha)$ and $E_2(\alpha)$ gateways are available for *every* combination of α and H_{lt} values depicted in Figure 4. Finally, note that a significant number of the LTPOs include an out-of-plane S^2 subspace, depicted by the black points, but the associated 3D motion is not leveraged in this investigation.

TRANSIT THROUGH E_1

A number of dynamical structures exist within the CR3BP-LT to guide low-thrust trajectories through the E_1 and E_2 gateways. The equilibria and the associated low-thrust gateway energies supply minimum H_{lt} values for transit as a function of α. Similarly, the manifolds associated with LTPOs located in the gateways act as separatrices between transit and non-transit motion and, thus, provide geometric bounds. To illustrate the application of such insights, consider a lunar mission with a spacecraft path that originates near the Earth (P_1 in the Earth-Moon CR3BP-LT) with a very

low H_{lt} value along a geostationary transit orbit (GTO). The first challenge is increasing the H_{lt} value such that transit through the E_1 gateway is possible. This challenge has been well studied by others and is not explored in detail here. To construct a reasonable set of initial conditions for the transit analysis, a set of trajectories are initialized at apogee on a GTO orbit with a variety of arguments of perigee. For simplicity, the GTO is assumed to be coplanar with the Earth-Moon orbital plane, i.e., the GTO is planar in the CR3BP-LT. Each initial state is propagated in the CR3BP-LT with a thrust magnitude of $f =$ 7e-2, an initial mass of $m = 1$, and a specific impulse of $I_{sp} = 3000$ seconds. The low-thrust acceleration vector is aligned with the velocity vector to maximize $\frac{\mathrm{d}H_{nat}}{\mathrm{d}t}$, resulting in an energy-optimal spiral departing the GTO state. Many other departure options are available (and, perhaps, even more mass-optimal), but this formulation proves sufficient to demonstrate a process that leverages low-thrust to achieve transit through the E_1 gateway to P_2.

To initiate the transit analysis, states along the spiral with $\dot{x} > 0$ are captured on the hyperplane, Σ_1, located on the yz-plane at $x = -\mu$. Although the spiral arcs are propagated with velocity-pointing thrust vectors, the control strategy may be adjusted at any time to achieve a goal other than escaping Earth's gravity well. A useful alternative is the control strategy that fixes $\vec{a}_{lt}$ in the rotating frame, yielding the autonomous, Hamiltonian system in which H_{lt} is an integral of the motion. The first requirement for transit through $E_1(\alpha)$ is that the low-thrust arc possesses a low-thrust Hamiltonian value greater than the gateway energy, i.e., $H_{lt} > H_{lt}\left(E_1(\alpha)\right)$. Since H_{lt} remains constant along low-thrust arcs using this fixed-$\vec{a}_{lt}$ strategy, manipulating H_{lt} to an appropriately large value at the Σ_1 map guarantees that the E_1 gateway remains open as long as $\vec{a}_{lt}$ is not modified en route to E_1. Recall that H_{lt}, described in Equation (8), is a function of H_{nat}, $\vec{r}$, and $\vec{a}_{lt}$. The H_{nat} value cannot be instantaneously changed without an impulsive $\Delta\vec{v}$, and $\vec{r}$ cannot be manipulated. However, the α angle that orients $\vec{a}_{lt}$ may be adjusted to achieve a different H_{lt} value. Accordingly, a *control curve* is formulated to describe the range of attainable H_{lt} values as a function of α,

$$\mathcal{U}_i(\alpha) : H_{lt} = H_{nat,i} - a_{lt}(x_i \cos\alpha + y_i \sin\alpha), \tag{20}$$

where $H_{nat,i}$ is the natural Hamiltonian value at the map crossing,

$$\vec{q}_i = \begin{Bmatrix} x_i & y_i & 0 & \dot{x}_i & \dot{y}_i & 0 \end{Bmatrix}^T. \tag{21}$$

The $\vec{q}_i$ points are filtered by H_{nat} to include only crossings with $-1.6 \leq H_{nat,i} \leq -1.45$, as plotted in Figure 5(a). This range generally yields curves that pass above the $\mathbb{E}_1$ energy curve, plotted in Figure 5(b). Some of these control curves, colored cyan to indicate low H_{nat} values, only pass above the $\mathbb{E}_1$ energy curve for a small range of α values. Higher-energy curves, such as those with $H_{nat} \approx -1.5$, lie entirely above the $\mathbb{E}_1$ energy curve, indicating that any α value is available to orient $\vec{a}_{lt}$ while maintaining an open E_1 gateway.

While the control curves in Figure 5(b) provide energy information to guide the transit design, additional geometric information is required; an H_{lt} value above the E_1 gateway energy is a necessary condition for transit, but is not sufficient. Recall that the manifolds associated with an LTPO, one located in a gateway, bound transit motion through the gateway. Thus, to transit the E_1 gateway, a $\vec{q}_i$ point must lie *inside* a stable manifold associated with an E_1 LTPO, $\Gamma_1(\alpha, H_{lt})$. To compute such a manifold, W, a set of arcs are propagated from Γ_1. Each arc is initialized by perturbing a fixed point, located at time τ relative to the $\tau = 0$ point on Γ_1, along the stable or unstable eigenvector of $\mathbf{\Phi}(\tau + T, \tau)$. The arcs are then propagated in forward or reverse time to asymptotically depart Γ_1. For example, the stable manifold plotted in Figure 6(a), W_1^{S-}, asymptotically approaches the E_1

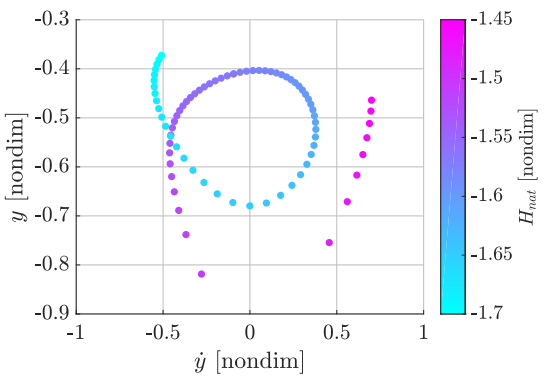

(a) Spiral states on Σ_1, colored by H_{nat}

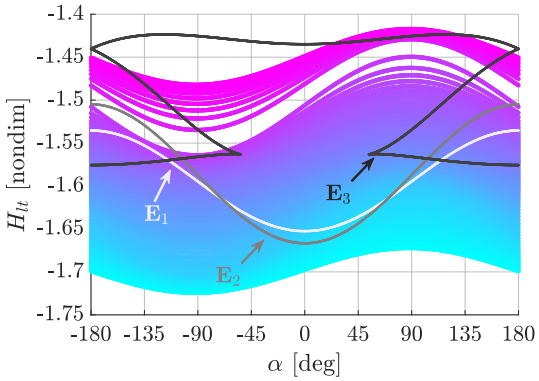

(b) Control curves for each spiral state, colored by H_{nat}

Figure 5. States on energy-optimal spirals from GTO apogee states with various arguments of perigee are captured on the Σ_1 Poincaré map; each point on the map is also represented as a control curve to identify LTPOs that facilitate transit through the E_1 gateway.

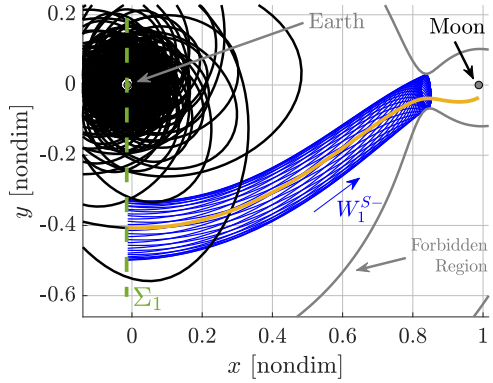

(a) The spiral trajectory (black) and manifold (blue) interface at the Σ_1 hyperplane

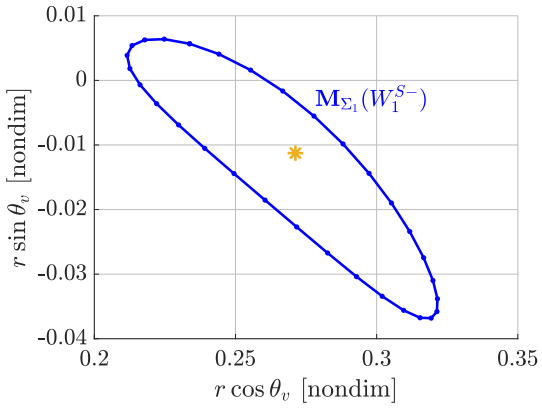

(b) Tube topology representation of the manifold (blue) and transit arc (yellow asterisk)

Figure 6. A transit arc (yellow) is identified at the Σ_1 map in the Earth-Moon CR3BP-LT with $a_{lt} = 7$e-2, $\alpha = -76.36°$, and $H_{lt} = -1.604$

LTPO, $\Gamma_1(76.36°, -1.604)$, from the negative $\hat{x}$-direction. All arcs that pass through the E_1 gateway with $\alpha = 76.36°$ and $H_{lt} = -1.604$ are bounded by W_1^{S-}. Thus, the next step is to determine the spiral trajectory map states that lie within W_1^{S-}.

To identify an intersection between a spiral trajectory map crossing, $\vec{q}_i$, and W_1^{S-}, the points on the $\mathcal{U}_i$ control curve are employed. For α values that yield $\mathcal{U}_i(\alpha) \geq H_{lt}\left(E_1(\alpha)\right)$, the $\Gamma_1\left(\alpha, \mathcal{U}_i(\alpha)\right)$ orbit is constructed and the associated W_1^{S-} manifold is propagated to the Σ_1 hyperplane for comparison with $\vec{q}_i$. The hyperplane fixes the x-coordinate, with three variables (y_i, $\dot{x}_i$, and $\dot{y}_i$) remaining for representation on the map. However, because the H_{lt} value associated with $\vec{q}_i$ may be manipulated (via $\mathcal{U}_i$) to be identical to the H_{lt} value associated with W_1^{S-}, the Hamiltonian may be leveraged to further reduce the number of free variables to two. The velocity magnitude is extracted from H_{lt} by solving Equation (7) for v. Thus, the remaining free variables, y_i and

$\theta_{v,i} = \arctan(\dot{y}_i/\dot{x}_i)$, are visualized via a "tube topology" transformation.[8,14] Polar coordinates are employed to avoid discrete jumps of 360° in θ_v, and the y-coordinate is scaled by the geometry of the low-thrust forbidden region to yield a radius,

$$r = \frac{y - \tilde{y}_l}{\tilde{y}_u - \tilde{y}_l}\,, \tag{22}$$

where $\tilde{y}_u$ and $\tilde{y}_l$ are the y-values of the forbidden region boundaries closest to the $\hat{x}$-axis at Σ_1, as illustrated in Figure 8(a). Let this transformation be combined with the Poincaré mapping via the operator,

$$\mathbb{M}^p_{\Sigma_1}(W) \coloneqq W \mapsto \mathbb{M}^p_{\Sigma_1}(W), \tag{23}$$

where W is a manifold (this mapping also applies to single states like $\vec{q}_i$), and p represents the p^{th} map iteration. (If the p superscript is omitted, $p = 1$ is implied.) Equivalently, $\mathbb{M}^p_{\Sigma}(W)$ captures the p^{th} return of W to Σ and incorporates a two-dimensional representation of W in the tube topology.

Once the spiral trajectory map crossing, $\vec{q}_i$, and the manifold, W_1^{S-}, are represented in the tube topology on Σ_1, identifying a transit arc is straightforward. If $\mathbb{M}_{\Sigma_1}(\vec{q}_i)$ is encircled by $\mathbb{M}_{\Sigma_1}(W_1^{S-})$, the low-thrust trajectory propagated from $\vec{q}_i$ with the selected α angle remains bounded by W_1^{S-} and the trajectory passes through the E_1 gateway. An example of this behavior is illustrated in Figure 6, with the spiral trajectory plotted in black, W_1^{S-} plotted in blue, and the transit arc plotted in yellow. Note that this example represents one possible α and H_{lt} combination on $\mathcal{U}_i$; additional points along $\mathcal{U}_i$ must be compared to LTPOs characterized by consistent α and H_{lt} values. Accordingly, to evaluate the transit possibilities for the entire set of spiral trajectories represented in Figure 5(a), a control curve is constructed for each $\vec{q}_i$, and points along that curve are compared to a matching W_1^{S-} manifold. The result of this search, visualized in Figure 7, identifies α values for each $\vec{q}_i$ that will deliver the spacecraft through the $E_1(\alpha)$ gateway. In this energy-space representation, each

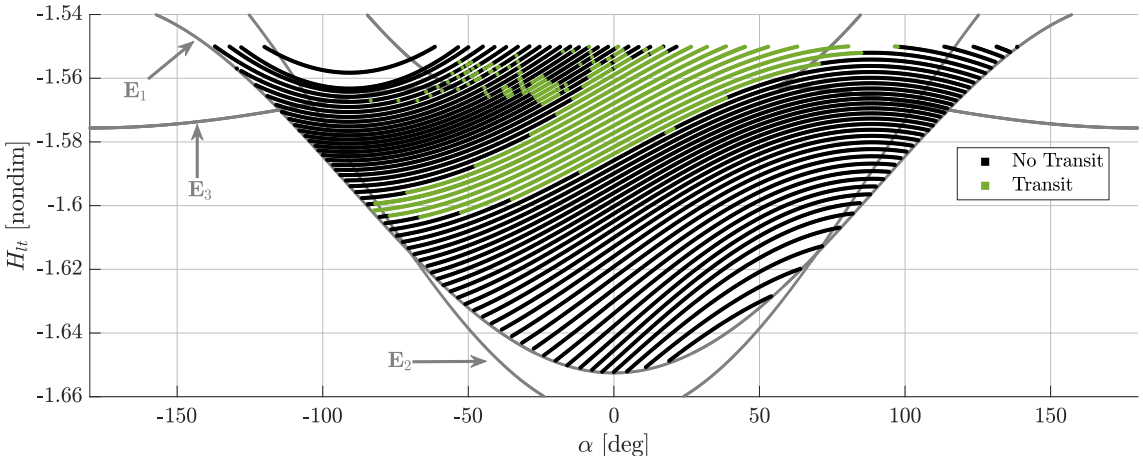

Figure 7. Sinusoidal control curves colored by their ability to transit the E_1 gateway; only a subset of the curves, and a subset of the α values on those curves, successfully deliver a transit arc.

sinusoidal curve is a control curve, $\mathcal{U}_i$, linked to a distinct four-dimensional map state, $\vec{q}_i$. Many of these curves are colored black for all α values, indicating that the associated $\vec{q}_i$ point cannot deliver the spacecraft to the P_2 region. However, a subset of the control curves do include feasible transit options, plotted in green. Each of these points represents an arc that origatinates from the associated

$\vec{q}_i$ state and, when propagated with the specified α value, transits the E_1 gateway. A comparison of the feasible transfer options between Figures 5(b) and 7 demonstrates that the number of transit options is greatly reduced when geometry is considered in addition to energy. However, recall that this analysis leverages only one set of initial conditions: energy-optimal spirals that originate at apogee on a GTO. Many other options exist to deliver a spacecraft from a low-energy state near the Earth to higher-energy states capable of reaching the Moon; this analysis can be applied to any such scheme. Additionally, these strategies may be reversed to identify regions to be used as targets for Earth-departing trajectories that enable transit.

TRANSIT AND CAPTURE IN THE P_2 REGION

Once a spacecraft has passed through the E_1 gateway, a new challenge emerges: navigating the nonlinear dynamics of the P_2 region. Once again, invariant manifolds associated with low-thrust periodic orbits (LTPOs) are employed to guide arcs through the region. An additional passage through the E_2 gateway constitutes a transit of the P_2 region, while arcs that remain near P_2 are denoted as "captured," at least for some finite time. As captured trajectories are merely those that do not transit, both possibilities are explored via the same analyses. The strategies employed to navigate the P_2 region are similar to those previously discussed, but include additional algorithmic complexity to compensate for the nonlinearities near P_2.

Algorithms for Transit Detection

Just as all arcs that originate in the system interior and pass through the E_1 gateway are bounded by W_1^{S-}, arcs that continue through the gateway into the P_2 region are bounded by W_1^{U+}. Similarly, trajectories that reach the system exterior via the E_2 gateway are bounded by W_2^{S-}. Recall that Γ_1 and Γ_2 orbits possess these manifolds for all α and H_{lt} values of interest, as illustrated by the existence of a saddle mode for every orbit in Figure 4. Accordingly, every combination of α and H_{lt} that lies above the $\mathbb{E}_1$ and $\mathbb{E}_2$ energy curves may permit transit through the P_2 region as the necessary manifolds exist and the H_{lt} value guarantees that both gateways are open. However, similar to the E_1 transit scenario described in the previous section, geometry must also be considered. A trajectory that passes through both gateways must be bounded by W_1^{U+} *and* by W_2^{S-}. To illustrate the process of locating transit arcs, consider a scenario in the Earth-Moon CR3BP-LT with $a_{lt} = 7\text{e-}2$, an α value of $-76.5°$, and $H_{lt} = -1.604$. The E_1 LTPO, $\Gamma_1(-76.5°, -1.604)$ (plotted in purple in Figure 8(a)), and the associated stable manifold, W_1^{U+} (plotted in red) bound motion that flows through E_1 toward the Moon. Similarly, $\Gamma_2(-76.5°, -1.604)$ (plotted in cyan in Figure 8(a)) and the associated W_2^{S-} manifold (plotted in blue), bound arcs that flow through the E_2 gateway to the system exterior. A new hyperplane, Σ_2, located at $x = 1 - \mu$ and plotted as a black, dashed line, is employed to compare the manifolds. Because both manifolds are characterized by the same α and H_{lt} values, the manifolds are reduced to two dimensions and represented in the tube topology via the same process outlined previously. The usefulness of this mapping, represented by the $\mathbb{M}_{\Sigma_2}$ operator, is clear when comparing the two manifold representations. While the W_1^{U+} and W_2^{S-} manifolds may seem to intersect in position space at Σ_2 in Figure 8(a), this xy-projection of the manifolds does not include velocity information and the manifolds do not truly intersect. The separation between the manifolds is obvious when the mapping is applied, as plotted in Figure 8(b): the $\mathbb{M}_{\Sigma_2}(W_1^{U+})$ and $\mathbb{M}_{\Sigma_2}(W_2^{S-})$ curves do not intersect.

While there is no intersection at the first map iteration of the two manifolds, propagating for additional returns may yield intersections. For example, when the map is iterated twice more, as plotted

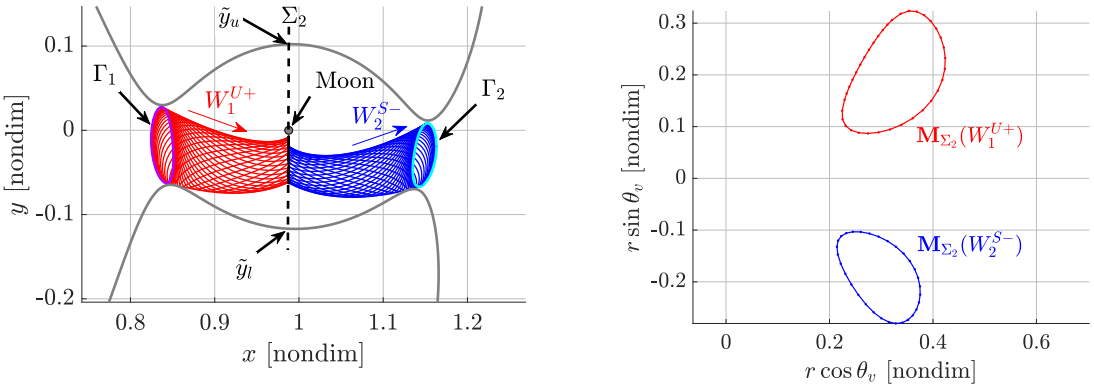

(a) Position Space: The xy-plane

(b) Poincaré Map in Tube Topology

Figure 8. Unstable (red) and stable (blue) manifolds are propagated from $\Gamma_1(-76.5°, -1.604)$ and $\Gamma_2(-76.5°, -1.604)$ LTPOs in the Earth-Moon CR3BP-LT with $a_{lt} = 7$e-2 to the Σ_2 hyperplane at $x = 1 - \mu$.

in Figure 9, an intersection occurs between $\mathbb{M}^3_{\Sigma_2}(W_1^{U+})$ and $\mathbb{M}^3_{\Sigma_2}(W_2^{S-})$. This change underscores

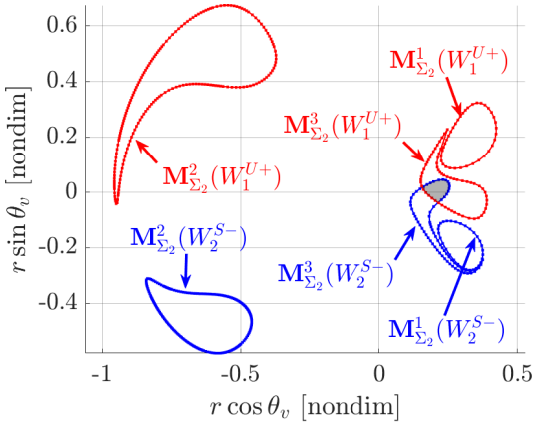

Figure 9. Three iterations of the map, represented in tube topology, capture unstable (red) and stable (blue) manifolds in the Earth-Moon CR3BP-LT with $a_{lt} = 7$e-2, $\alpha = -76.5°$, and $H_{lt} = -1.604$

an important caveat to the intersection analyses: a lack of intersections between manifolds does not support a conclusion that no transit motion exists. While the results plotted in Figure 8(b) may lead to a claim that transit is not possible with the given a_{lt}, α, and H_{lt} combination, it is clear an intersection does exist when additional map iterations are included. Only a few specific insights are available from the maps in Figures 8(b) and 9. First, arcs within the intersection regions, such as the point marked by an orange asterisk in Figure 10(a), are guaranteed to transit the P_2 region in the time prescribed by the manifolds bounding the arc. Since this arc is bounded by the third map iteration of each manifold, the trajectory, plotted in orange in Figure 10(b), includes five crosses through the Σ_2 hyperplane: three crossings for each manifold, with one shared between the manifolds. A second guarantee is that arcs along a manifold, such as the blue asterisk on $\mathbb{M}^3_{\Sigma_2}(W_2^{S-})$ in Figure 10(a), will remain on the manifold and will asymptotically approach the associated periodic orbit. Because a portion of $\mathbb{M}^3_{\Sigma_2}(W_2^{S-})$ lies within $\mathbb{M}^3_{\Sigma_2}(W_1^{U+})$, arcs from the system interior (e.g., the

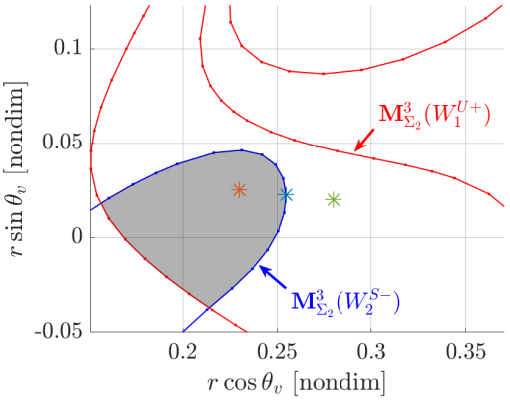

(a) Three states are selected on the map within the third map iterations of one or both of the manifolds (zoomed-in view of Figure 9)

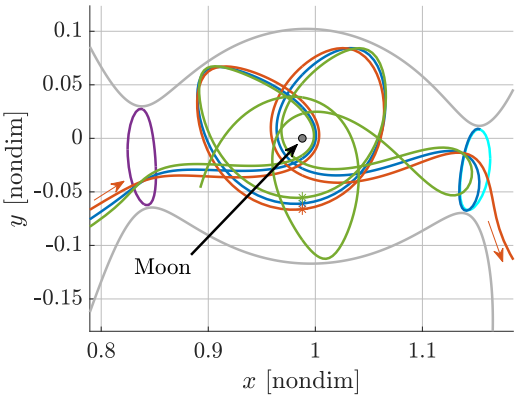

(b) The trajectories that result from the selected map states; the map states are again located by asterisks

Figure 10. A transit trajectory (orange), a trajectory to Γ_2 (blue), and a captured trajectory (green) in the Earth-Moon CR3BP-LT with a_{lt} = 7e-2, $\alpha = -76.5°$ and $H_{lt} = -1.604$

blue trajectory plotted in Figure 10(b) that is associated with the blue asterisk map state) may transit the E_1 gateway within W_1^{U+} and also reach Γ_2. In essence, this scenario represents a capture as the spacecraft remains on Γ_2, near P_2, as long as the α angle is maintained. Finally, some insights regarding non-transit motion is also available from the map. Consider a state within W_1^{U+} (capable of transit into the P_2 region via the E_1 gateway) but not within W_2^{S-}, such as the state located by the green asterisk in Figure 10(a). The corresponding trajectory cannot pass through the E_2 gateway before crossing Σ_2 at least twice, i.e., the trajectory may pass through the E_2 gateway after crossing Σ_2 three or more times. Additionally, the trajectory may return to the system interior via the E_1 gateway if the green asterisk lies within any mappings of W_1^{S+} (not included in the plots). This non-transit path, plotted in green in Figure 10(b), crosses Σ_2 five times after passing through $\mathbb{M}^3_{\Sigma_2}(W_2^{S-})$ and additional crossings of Σ_2 may occur if propagated for a longer interval.

While the overall behavior of the three arcs depicted in Figure 10 are very different, the initial conditions that are selected from the map are located very close to one another. Each arc originates on Σ_2 with a similar θ_v angle and slightly different r values (that translate to different y values). When propagated in reverse time, these states yield arcs that remain near one another and pass through the E_1 gateway. When propagated in forward time, the arcs maintain similar geometries until they reach Γ_2, plotted in cyan in Figure 10(b). At this point, the red arc passes through the gateway, the blue arc asymptotically approaches Γ_2, and the green arc returns toward P_2. Without the manifolds to differentiate these behaviors, the path of each arc is difficult to predict. Additionally, the same techniques may be leveraged in other applications, such as the identification heteroclinic connections between the two LTPOs[15], or the determination of arcs that do not transit either gateway. It is apparent that the manifolds associated with the gateway LTPOs serve as useful structures to differentiate many types of motion.

Global Transit Search

To determine the combinations of α and H_{lt} that permit transit, as well as the details of each transit opportunity, the process of identifying intersections between manifolds is automated to evaluate

the criteria over the grid of α and H_{lt} values that satisfy the gateway energy constraints. For each combination:

1. Compute the low-thrust periodic orbits, $\Gamma_1(\alpha, H_{lt})$ and $\Gamma_2(\alpha, H_{lt})$.

2. Construct an initial representation of W_1^{U+} and W_2^{S-} with a small number of arcs (31 are used per orbit to minimize the computation time) and iterate the map n times, yielding the mappings $\mathbb{M}^p_{\Sigma_2}(W_1^{U+})$ and $\mathbb{M}^p_{\Sigma_2}(W_2^{S-})$ for $p = 1, 2, \ldots, n$. Note that, at some combinations of α and H_{lt}, a subset of the arcs along a manifold may not reach a map return; some escape through one of the gateways, while others reach the P_2 singularity, defined here as a state with $r_{23} <$ 5e-3 nondimensional units, or approximately 192 km in the Earth-Moon system. These arcs are excluded from the map iterations following the escape or crash "event" to avoid excessively long propagation times.

3. Fill "gaps" in each mapping, $\mathbb{M}^p_{\Sigma_2}(W)$. Gaps may occur when arcs on the manifold fail to reach the map, as described in the previous step. Gaps also occur due to the nonlinear dynamics in the CR3BP-LT. For example, while all of the arcs representing W may reach the map, they may not be uniformly distributed across the range of r and θ_v values. Large inter-arc differences in r or θ_v (θ_v almost always reflects the most uneven coverage) at Σ_2 can result in large distances between points on $\mathbb{M}^p_{\Sigma_2}(W)$. Gaps are filled via two techniques:

   a. *Discrete Fourier Series.* The y, $\dot{x}$, and $\dot{y}$ states that are used to construct $\mathbb{M}^p_{\Sigma_2}(W)$ are approximated via discrete Fourier series. (This choice of variables produces a more accurate approximation of $\mathbb{M}^p_{\Sigma_2}(W)$ than fitting the series directly to r and θ_v.) This Fourier scheme is only applied when $\mathbb{M}^p_{\Sigma_2}(W)$ is uniformly sampled in τ (the time-of-flight along Γ from $\tau = 0$ to the manifold arc "step-off" point), i.e., when all the arcs representing W reach the map. The Fourier representations of y, $\dot{x}$, and $\dot{y}$ states are transformed into the tube topology and compared to the data points on $\mathbb{M}^p_{\Sigma_2}(W)$. If the error exceeds a certain threshold, the Fourier representation is abandoned in favor of the second strategy. If the error in the approximation remains within the desired limits, points are selected from the Fourier approximations to minimize the maximum inter-point distance along $\mathbb{M}^p_{\Sigma_2}(W)$.

   b. *Interpolation and Propagation.* When $\mathbb{M}^p_{\Sigma_2}(W)$ is not uniformly sampled in τ, or when the Fourier series fail to accurately approximate $\mathbb{M}^p_{\Sigma_2}(W)$, additional points on $\mathbb{M}^p_{\Sigma_2}(W)$ are computed by propagating arcs from the originating periodic orbit, Γ, to the p^{th} map iteration. Points along Γ are selected between the τ values associated with the manifold arcs that bound large gaps on $\mathbb{M}^p_{\Sigma_2}(W)$. These initial conditions are then propagated and included in $\mathbb{M}^p_{\Sigma_2}(W)$ (assuming the arcs do not escape or impact P_2 before reaching the map). Gaps in $\mathbb{M}^p_{\Sigma_2}(W)$ are iteratively filled until all gaps are smaller than some tolerance, or until a maximum number of iterations occurs.

   If the gaps in $\mathbb{M}^p_{\Sigma_2}(W)$ cannot be filled, the p^{th} map iteration is abandoned and not incorporated in subsequent steps. This failure occurs more frequently at higher H_{lt} values where manifold arcs are more likely to escape or crash.

4. Compute intersecting regions between two manifold mappings, $\mathbb{M}^p_{\Sigma_2}(W_1^{U+})$ and $\mathbb{M}^k_{\Sigma_2}(W_2^{S-})$. If intersections exist, the bounds of the region, denoted $\mathbb{A}^{p,k}$, are extracted for further analysis.

Following the completion of these steps for the gridded α and H_{lt} values, several properties of the data are investigated.

As a first exploration of the transit options between E_1 and E_2 in the Earth-Moon CR3BP-LT with $a_{lt} = 7\text{e-}2$, consider a binary measure of "transitability." The p^{th} iteration of $\mathbb{M}_{\Sigma_2}(W_1^{U+})$ is compared with $\mathbb{M}_{\Sigma_2}^k(W_2^{S-})$ for $k = 1, \ldots, n$. The smallest k for which an intersection between manifolds occurs is captured and plotted for $p = 1, 2$, and 3 in Figure 11. Accordingly, each

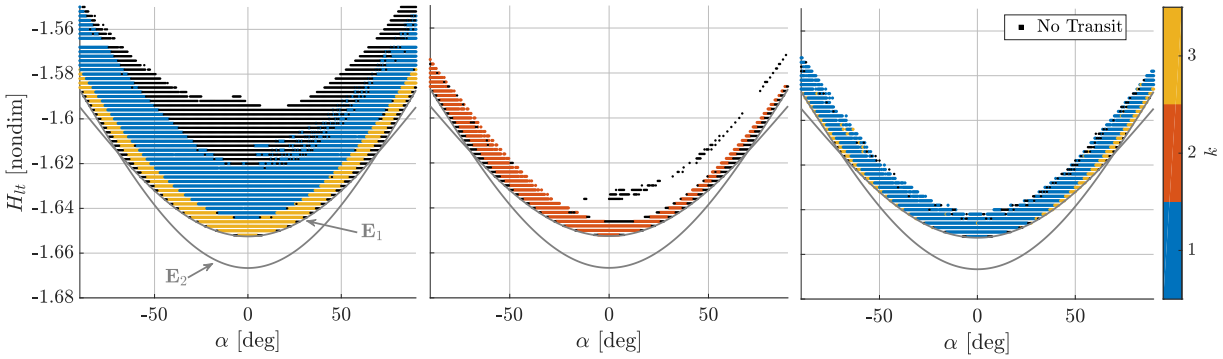

(a) $p = 1$ (b) $p = 2$ (c) $p = 3$

Figure 11. Earliest intersections of $\mathbb{M}_{\Sigma_2}^p(W_1^{U+})$ by $\mathbb{M}_{\Sigma_2}^k(W_2^{S-})$

plot in the figure depicts the most rapid (in terms of map iterations) transit opportunities for arcs within W_1^{U+} at each of the three map iterations. Black points indicate that no intersections exist between $\mathbb{M}_{\Sigma_2}^p(W_1^{U+})$ and $\mathbb{M}_{\Sigma_2}^k(W_2^{S-})$ for $k = 1, 2$, or 3. Empty space in each plot represents combinations of α and H_{lt} that cannot be analyzed, including areas above and below the $\mathbb{E}_1$ and $\mathbb{E}_2$ energy curves. Points below the energy curves do not possess H_{lt} values that are sufficiently high to open both gateways and are discarded from the search. However, the automated search considers all points above the curves, and the remaining empty regions are discarded due to failures to fill gaps in the mappings during step 3. The forbidden region geometries associated with these difficult combinations of α and H_{lt} frequently include wide gateways, thus, the arcs on the two manifolds are more likely to escape, particularly after the first map iteration. Additionally, many arcs along these manifolds pass near the P_2 singularity and, subsequently, are discarded. The combinations of α and H_{lt} most straightforwardly analyzed are those located near the $\mathbb{E}_1$ and $\mathbb{E}_2$ energy curves. These combinations are linked to geometries defined by the forbidden region boundaries with relatively narrow gateways; these dynamics yield manifolds that cross Σ_2 several times.

To understand the results in Figure 11, consider the transit example identified by the red arc in Figure 10(a) with $\alpha = -76.5°$ and $H_{lt} = -1.604$. In energy space, this trajectory is located very near the $\mathbb{E}_2$ energy curve, above and to the left of the intersection between the $\mathbb{E}_1$ and $\mathbb{E}_2$ curves. The mappings in Figure 9 demonstrate that the only manifold intersection for this configuration (for $p, k \leq 3$) occurs at $p = k = 3$. Thus, the α and H_{lt} combination is located in a black, no-transit, region in Figures 11(a) and 11(b) as neither $\mathbb{M}_{\Sigma_2}^1(W_1^{U+})$ nor $\mathbb{M}_{\Sigma_2}^2(W_1^{U+})$ intersects any of the W_2^{S-} map iterations. However, the corresponding region in Figure 11(c) is colored yellow to indicate that $\mathbb{M}_{\Sigma_2}^3(W_1^{U+})$ includes an intersection with $\mathbb{M}_{\Sigma_2}^k(W_2^{S-})$ for $k = 3$. Many of the points near the bounding $\mathbb{E}_1$ and $\mathbb{E}_2$ energy curves are characterized by similar trends: the first transit opportunity for these α and H_{lt} configurations occurs only after three map iterations of each manifold. However,

for configurations slightly further from the two energy curves, intersections occur earlier, yielding a smaller number of map iterations for those transits. For example, the yellow band in Figure 11(a) identifies α and H_{lt} configurations for which the first transit opportunity at $\mathbb{M}^1_{\Sigma_2}(W_1^{U+})$ occurs with $\mathbb{M}^3_{\Sigma_2}(W_2^{S-})$. As this sequence links the $p = 1$ map iteration and the $k = 3$ iteration, the total number of map iterations to complete the transit is $p + k - 1 = 3$, whereas the red trajectory from Figure 10(b) crosses Σ_2 five times.

The number of map iterations required to complete a transit is directly linked to the minimum time-of-flight (TOF) for the transit. A TOF metric for an intersection area, $\mathbb{A}^{p,q}$ is computed by averaging the TOF for the arcs on $\mathbb{M}^p_{\Sigma_2}(W_1^{U+})$ and $\mathbb{M}^k_{\Sigma_2}(W_2^{S-})$ that bound $\mathbb{A}^{p,k}$ and then summing the two averages. Although these minimum TOFs for each intersection, plotted in Figure 12, do not necessarily supply an accurate measure of the true TOF along any arc in $\mathbb{A}^{p,q}$, this approximation does facilitate comparisons between various α and H_{lt} combinations. For instance, the yellow

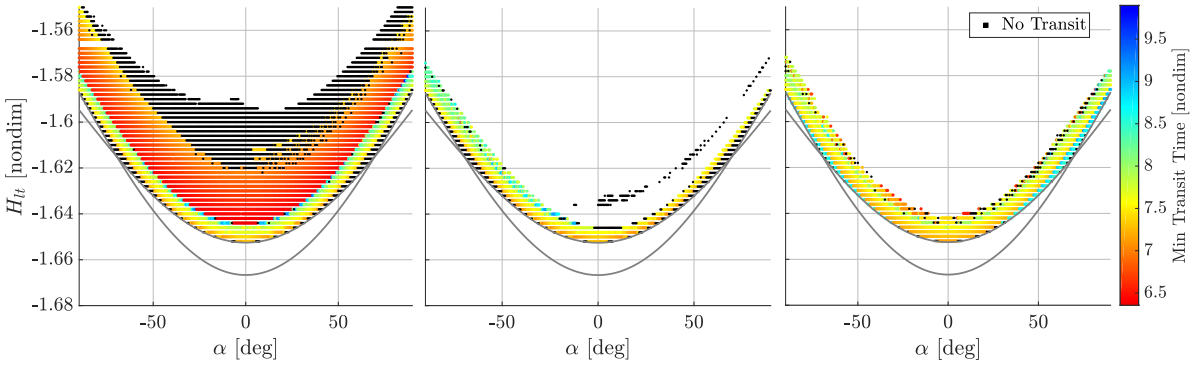

(a) $p = 1$ (b) $p = 2$ (c) $p = 3$

Figure 12. Minimum times-of-flight for intersections between $\mathbb{M}^p_{\Sigma_2}(W_1^{U+})$ and $\mathbb{M}^k_{\Sigma_2}(W_2^{S-})$ for $k = 1, 2,$ and 3

$(p = 1,\ k = 3)$ region in Figure 11(a), when mapped to the same α and H_{lt} values in Figure 12(a), corresponds to TOFs between 7.0 and 8.0 nondimensional time units (about 30-35 days in the Earth-Moon system). Similarly, the yellow $(p = 3,\ k = 3)$ region in Figure 11(c) corresponds to TOFs in Figure 12(c) between 8.5 and 9.0 (about 37-40 days). These TOFs are consistent with the TOFs for the red $(p = 2,\ k = 2)$ region in Figure 11(b) as well as with the TOFs for the blue $(p = 3,\ q = 1)$ region in Figure 11(c). This result is expected given that the total number of map iterations during the transit, $p+q-1$, is identical for all three of these regions. Thus, it is consistent that the shortest times-of-flight are associated with the $(p = 1,\ k = 1)$ region in Figure 11(a); the minimum TOF for this region is below 6.5 nondimensional time units, or less than 28 days.

Capture: Avoiding Transit

For many space missions, capture near P_2, e.g., the Moon in the Earth-Moon system, is desirable. Originating from the system interior, one strategy to capture near P_2 and avoid transit through the E_2 gateway is to select an α and H_{lt} configuration that lies below the $\mathbb{E}_2$ energy curve. As a result, the E_2 gateway remains closed as the spacecraft moves along the low-thrust arc into the P_2 region. Consider the configurations plotted in green in Figure 7 (reproduced in Figure 13(a)) that adjust the CR3BP-LT dynamics to allow a spacecraft to transition from the energy-optimal spiral to an arc

that transits the E_1 gateway: the majority of these configurations are located above the $\mathbb{E}_2$ energy curve, but a small number near $\alpha = -90^\circ$ and $H_{lt} = -1.6$ are located below the $\mathbb{E}_2$ energy curve. Selecting one of these configurations yields a transfer that cannot continue through the E_2 gateway. For example, selecting $\alpha = -80.86^\circ$ at Σ_1 results in a trajectory with $H_{lt} = -1.602$, plotted in yellow in Figure 13(b), that cannot escape through E_2 as the gateway is closed.

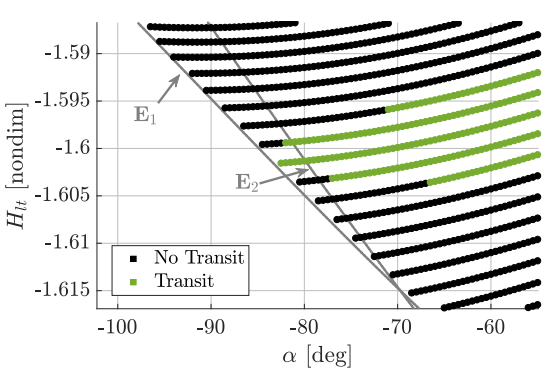

(a) A detailed view of transit options below the $\mathbb{E}_2$ energy curve

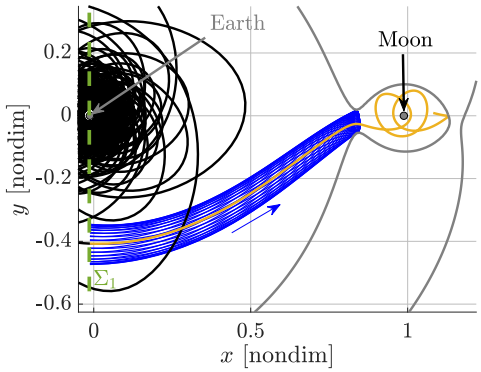

(b) Selecting $\alpha = -80.86^\circ$ at Σ_1 yields an arc with $H_{lt} = -1.602$ that transits E_1 but not E_2

Figure 13. A trajectory that captures near the Moon in the Earth-Moon CR3BP-LT for $a_{lt} = 7$e-2

While selecting α and H_{lt} values that lie below the $\mathbb{E}_2$ energy curve is sufficient to prohibit transit of the P_2 region, other non-transit options exist for configurations with both the E_1 and E_2 gateways open. For instance, the results in Figure 11 include regions of black, non-transit options located very near the $\mathbb{E}_1$ energy curve where the $\mathbb{E}_1$ and $\mathbb{E}_2$ energy curves intersect. These regions are large and visible at the scale depicted in Figures 11(a) and 11(b), but are very small in Figure 11(c). These latter results for $p = 3$, reproduced at a larger scale in Figure 14(a), also to include a set of non-transit options, colored black, near the intersection of the two energy curves. Selecting one

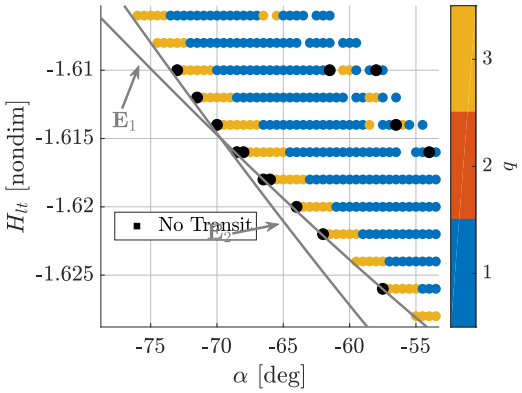

(a) Earliest intersections of $\mathbb{M}^3_{\Sigma_2}(W_1^{U+})$ by $\mathbb{M}^q_{\Sigma_2}(W_2^{S-})$; Some configurations, marked by black dots, do not include transit options for $k = 1, 2$, or 3

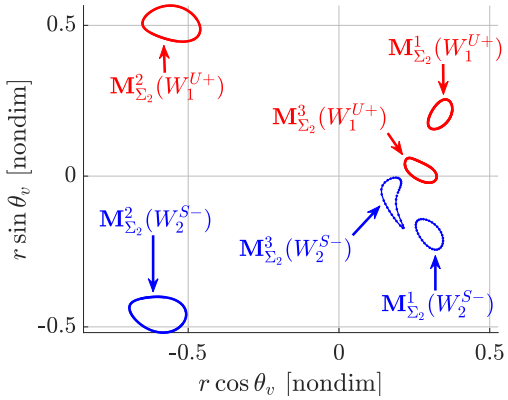

(b) The $\mathbb{M}^p_{\Sigma_2}(W_1^{U+})$ (red) and $\mathbb{M}^p_{\Sigma_2}(W_2^{S-})$ (blue) manifolds do not intersect for $p = 1, 2$, or 3 with $\alpha = 70^\circ$ and $H_{lt} = -1.614$

Figure 14. Although both the E_1 and E_2 gateways are open, some α and H_{lt} configurations do not include transit options in the Earth-Moon CR3BP-LT for $a_{lt} = 7$e-2

of these configurations yields a map with no intersections between manifold mappings, as depicted in Figure 14(b) for $\alpha = 70^\circ$ and $H_{lt} = -1.614$. Thus, an arc that passes through the E_1 gateway, i.e., through the red W_1^{U+} mappings, will not exit through the E_2 gateway for the given number of map iterations (in this case, three). Although both of these strategies supply only a limited number of options to avoid transiting E_2, this limitation may benefit the design process by narrowing the number of control parameters. Finally, a third strategy to avoid transit leverages the control curves introduced in the "Transit Through E_1" section to select points along a low-thrust trajectory where α may be modified to close one or both of the gateways; the details of such a design are available in previous efforts.[8] At each point along a low-thrust arc, a control curve may be constructed to describe the range of attainable H_{lt} values. If the control curve includes points below the $\mathbb{E}_1$ or $\mathbb{E}_2$ energy curve(s), then the E_1 or E_2 gateway(s) may be closed, bounding the resulting low-thrust motion inside the P_2 region.

CONCLUDING REMARKS

Dynamical structures within the CR3BP-LT, including low-thrust forbidden regions, low-thrust periodic orbits, and the manifolds associated with the periodic orbits, bound trajectories that transit through gateways near P_2. Several strategies are developed to leverage these structures and other insights from the CR3BP-LT to design trajectories that either transit the P_2 region or reach the P_2 region and then remain captured. As in many low-thrust design problems, one key challenge is the selection of low-thrust control parameters along the trajectory. Control curves that link the control parameters with the energy of a low-thrust arc supply an initial set of bounds on feasible parameters for transit and capture, while the manifolds associated with low-thrust periodic orbits supply additional bounds that accommodate the geometry of the trajectories. Algorithms that leverage these insights are designed and applied to explore a variety of control parameter configurations. The results demonstrate that many options for transit and capture exist, but are significantly more limited than predicted solely by an energy analysis, i.e., incorporating the manifold geometry is an important step in selecting control parameters for transit and capture trajectories. While optimality is not directly considered, these preliminary efforts to explore the trade space may be leveraged in future investigations with a stronger emphasis on propellant consumption or time-of-flight.

ACKNOWLEDGMENTS

The authors wish to thank the Purdue University School of Aeronautics and Astronautics for the facilities and support, including access to the Rune and Barbara Eliasen Visualization Laboratory. Additionally, many thanks to the Purdue Multi-Body Dynamics Research Group for interesting discussions and ideas. This research is supported by a National Aeronautics and Space Administration (NASA) Space Technology Research Fellowship, NASA Grant NNX16AM40H.

REFERENCES

[1] N. Bosanac, A. D. Cox, K. C. Howell, and D. C. Folta, "Trajectory Design for a Cislunar CubeSat Leveraging Dynamical Systems Techniques: The Lunar IceCube Mission," *Acta Astronautica*, Vol. 144, Mar. 2018, pp. 283–296.

[2] C. Conley, "Low Energy Transit Orbits in the Restricted Three-Body Problem," *Society for Industrial and Applied Mathematics Journal on Applied Mathematics*, Vol. 16, 1968, pp. 732–746.

[3] W. S. Koon, M. W. Lo, J. E. Marsden, and S. D. Ross, "Low Energy Transfer to the Moon," *Celestial Mechanics and Dynamical Astronomy*, Vol. 81, 2001, pp. 63–73.

[4] G. Gómez, W. Koon, M. Lo, J. Marsden, J. Masdemont, and S. Ross, "Connecting orbits and invariant manifolds in the spatial restricted three-body problem," *Nonlinearity*, Vol. 17, No. 5, 2004, pp. 1571–1606.

[5] G. Mingotti, F. Topputo, and F. Bernelli-Zazzera, "Low-Energy, Low-Thrust Transfers to the Moon," *Celestial Mechanics and Dynamical Astronomy*, Vol. 105, 2009, pp. 61–74.

[6] R. Anderson and M. Lo, "Role of Invariant Manifolds in Low-Thrust Trajectory Design," *Journal of Guidance, Control, and Dynamics*, Vol. 32, Nov. 2009, pp. 1921–1930.

[7] M. Morimoto, H. Yamakawa, and K. Uesugi, "Periodic Orbits with Low-Thrust Propulsion in the Restricted Three-Body Problem," *Journal of Guidance, Control, and Dynamics*, Vol. 29, Sept. 2006.

[8] A. D. Cox, K. C. Howell, and D. C. Folta, "Dynamical Structures in a Low-Thrust, Multi-Body Model with Applications to Trajectory Design," *Celestial Mechanics and Dynamical Astronomy*, (accepted).

[9] V. Szebehely, *Theory of Orbits: The Restricted Problem of Three Bodies*. New York: Academic Press, 1967.

[10] A. D. Cox, K. C. Howell, and D. C. Folta, "Dynamical Structures in a Combined Low-Thrust Multi-Body Environment," *AAS/AIAA Astrodynamics Specialist Conference*, Columbia River Gorge, Stevenson, Washington, Aug. 2017.

[11] A. Farrés, "Transfer orbits to L4 with a solar sail in the Earth-Sun system," *Acta Astronautica*, Vol. 137, 2017, pp. 78–90.

[12] A. D. Cox, K. C. Howell, and D. C. Folta, "Trajectory Design Leveraging Low-Thrust, Multi-Body Equilibria and Their Manifolds," *AAS/AIAA Astrodynamics Specialist Conference*, Snowbird, Utah, Aug. 2018.

[13] C. Simó, G. Gómez, J. Llibre, R. Martínez, and J. Rodríguez, "On the optimal station keeping control of halo orbits," *Acta Astronautica*, Vol. 15, June 1987, pp. 391–397.

[14] T. Swenson, M. W. Lo, B. Anderson, and T. Gordordo, "The Topology of Transport Through Planar Lyapunov Orbits," *AIAA SciTech Forum*, Kissimmee, Florida, Jan. 2018.

[15] A. F. Haapala and K. C. Howell, "A Framework for Construction of Transfers Linking Periodic Libration Point Orbits in the Earth-Moon Spatial Circular Restricted Three-Body Problem," *Journal of Bifurcations and Chaos*, Vol. 26, May 2016.